

# 3D Microstructured Frequency Selective Surface Based on Carbonized Polyimide Films for Terahertz Applications

May Zin Hlaing, Vaithinathan Karthikeyan, Wei Wu, Bao Jie Chen, Aaron Kubong Ng, Chi-Hou Chan, Maria Merlyne De Souza, and Vellaisamy A. L. Roy\*

In recent years, frequency selective surface (FSS)-based two-dimensional (2D) and three-dimensional (3D) carbon materials such as carbon nanofibers, carbon nanotubes, and carbon-filled filaments are essential tools to design millimeter-wave radomes, absorbers, electromagnetic interference (EMI) shielding, and antenna reflectors in gigahertz (GHz) regimes. Terahertz (THz) technologies are gaining attentions from medical imaging to security surveillance. In this work, a 3D microstructured FSS using carbon-based polyimide as a precursor to enhance the resonant frequency at the THz range. Furthermore, gold nanoparticles (AuNPs) are embedded on 3D microstructured carbonized polyimide (3D-CPI) film to improve their FSS property through plasmonic effects. From the time domain spectroscopy measurements, 3D-CPI FSS film shows band-stop filter properties in the frequency range of 0.5–1.5 THz and with a maximum return loss (RL) of 40.5 dB (at the resonant frequency of 1 THz). The 3D-CPI/AuNPs film demonstrates the highest RL of 43.7 dB at the higher excitation resonance frequency  $\approx 1.06$  THz due to the interaction of plasmonic electrons with scattered delocalized electrons in carbon, which induces the mechanisms for EMI shielding. The results will open insight into 3D plasmonic carbon microstructures as an EMI shielding material at THz frequency.

## 1. Introduction

Frequency selective surfaces (FSS) consist of a periodic arrangement of 1D or 2D metallic structures that drew significant attention owing to their frequency resonating property. An FSS can reflect (band-stop) or transmit (band-pass) the incoming EM wave selectively in specific frequency ranges according to their size, shape, thickness, and other parameters, which are the identifying features of FSS.<sup>[1]</sup> Metallic and dielectric material structures are widely used to design terahertz FSS or filters as they possess high mechanical strength, which helps produce functionalized designs. Metallic FSSs can shield by reflecting or absorbing the electromagnetic interference, however, which are costly to manufacture as desired structures and are being substituted by carbon-based materials for electromagnetic properties at high frequencies with suitable cost, lightweight, and corrosion-


free.<sup>[2]</sup> Generally, Carbon-based materials are  $sp$ ,  $sp^2$ , and  $sp^3$ -bonded, forming long chains of interconnecting carbon-carbon bonds resulting in differing physical and electrical properties.<sup>[3]</sup> Hence, such materials can be classified as semimetals or non-dielectric materials (such as graphene, graphite, carbon nanotubes, carbon nanofibers)<sup>[4,5]</sup> therefore exhibiting THz optical transition, optoelectronic properties, and dielectric properties in their nanocomposites by the generation of THz pulses from the application of femtosecond laser pulses in magnetic and electric fields.<sup>[6–11]</sup> These carbon-based materials show an excellent EMI shielding performance due to the presence of delocalized  $\pi$ -bond electrons. The freely moving electrons interact with the EM wave leading to reflection with maximum return loss values at the resonating frequency.<sup>[12]</sup> The excessive energy of EM can damage the surrounding circuits and induce unnecessary noise pulse. Liang et al. reported bamboo-like short carbon fibers@ $Fe_3O_4$ @phenolic resin and honeycomb-like short carbon fibers@ $Fe_3O_4$ @ $FeO$  composites as high-performance EM wave absorbing materials successfully achieving reflection loss  $-10$  dB at 4–18 GHz range.<sup>[13]</sup> However, the characterization of carbon-based materials under the THz regime is still not well accounted for in the literature, with very few reports on the FSS property of carbon-based materials. Recently, a carbon-based FSS absorber fabricated by using 3D-printing

M. Z. Hlaing, V. Karthikeyan, W. Wu  
State Key Laboratory for Terahertz and Millimeter Waves  
Department of Materials Science & Engineering  
City University of Hong Kong  
Kowloon, Hong Kong, China

B. J. Chen, A. K. Ng, C.-H. Chan  
State Key Laboratory for Terahertz and Millimeter Waves  
Department of Electrical Engineering  
City University of Hong Kong  
Kowloon, Hong Kong, China

M. M. De Souza  
Electronic and Electrical Engineering  
University of Sheffield  
North Campus, Sheffield S3 7HQ, UK

V. A. L. Roy  
James Watt School of Engineering  
University of Glasgow  
Glasgow G12 8QQ, UK  
E-mail: val.roy@cityu.edu.hk

 The ORCID identification number(s) for the author(s) of this article can be found under <https://doi.org/10.1002/adom.202102178>.

© 2022 The Authors. Advanced Optical Materials published by Wiley-VCH GmbH. This is an open access article under the terms of the Creative Commons Attribution License, which permits use, distribution and reproduction in any medium, provided the original work is properly cited.

DOI: 10.1002/adom.202102178

technology is favored due to easily control the functionalized structures and use suitable precursors. Huang et al. reported the review of 3D-printing technology that fabricates complex structures using lightweight materials by achieving better EM absorption performance.<sup>[14]</sup> Mi et al. reported 3D printing FSS electromagnetic absorber based on conductive carbon-filled filament obtaining multiple resonances of the reflection coefficient at 1–18 GHz range.<sup>[15]</sup> Jaiswar et al. studied the inkjet-printed FSS based on CNT for ultra-wideband thin microwave absorber at 7–50 GHz.<sup>[16]</sup> Based on the previous studies, we explore the behavior of a potential 3D FSS carbon-based material at the terahertz range. In this work, we design 3D microstructured FSS carbon-based materials using polyimides as carbon precursors that have advantages with excellent physical properties, which after carbonization and graphitization, give a high carbon yield and electrical conductivity equivalent to graphitic carbon.<sup>[17]</sup> 3D microstructured FSS is fabricated by using the molding techniques to easily control the shape of desired structure and using the molding techniques can comfortably modify the concentration of carbon precursors. Kapton, a well-known commercial polyimide material with repeated units of PMDA/ODA, was shown to demonstrate optical properties such as transmission, reflection, and absorption in GHz range without any

resonance frequencies by Venkatachalam et al.<sup>[18]</sup> To understand the interaction between the chemical bonds, Zhang et al. studied the carbon-based materials for their THz transmission properties.<sup>[19]</sup> We also compare the THz-FSS properties in planar carbonized polyimide films (CPI-planar) and 3D microstructured carbonized polyimide (3D-CPI) films to enhance the resonance frequency, and these when embedded with Au nanoparticles, increase the enhancement of the resonance frequency via the plasmonic effect. Thus, we design and demonstrate effective 3D pyramidal microstructured carbon films as an effective terahertz frequency selective surface (Band Stop Filter) with maximum return loss in the range of 0.5–1.1 THz.

## 2. Results and Discussion

Figure 1a illustrates the design, fabrication, and conversion of 3D microstructured FSS polyimide (PI) film into metallic carbon (CPI) film after carbonization at 1600 °C. Gold nanoparticles (AuNPs) are deposited onto the carbonized 3D microstructured CPI film to experience the plasmonic effect and enhance FSS performance. A sequentially controlled temperature profile is required to achieve the metallic conduction in

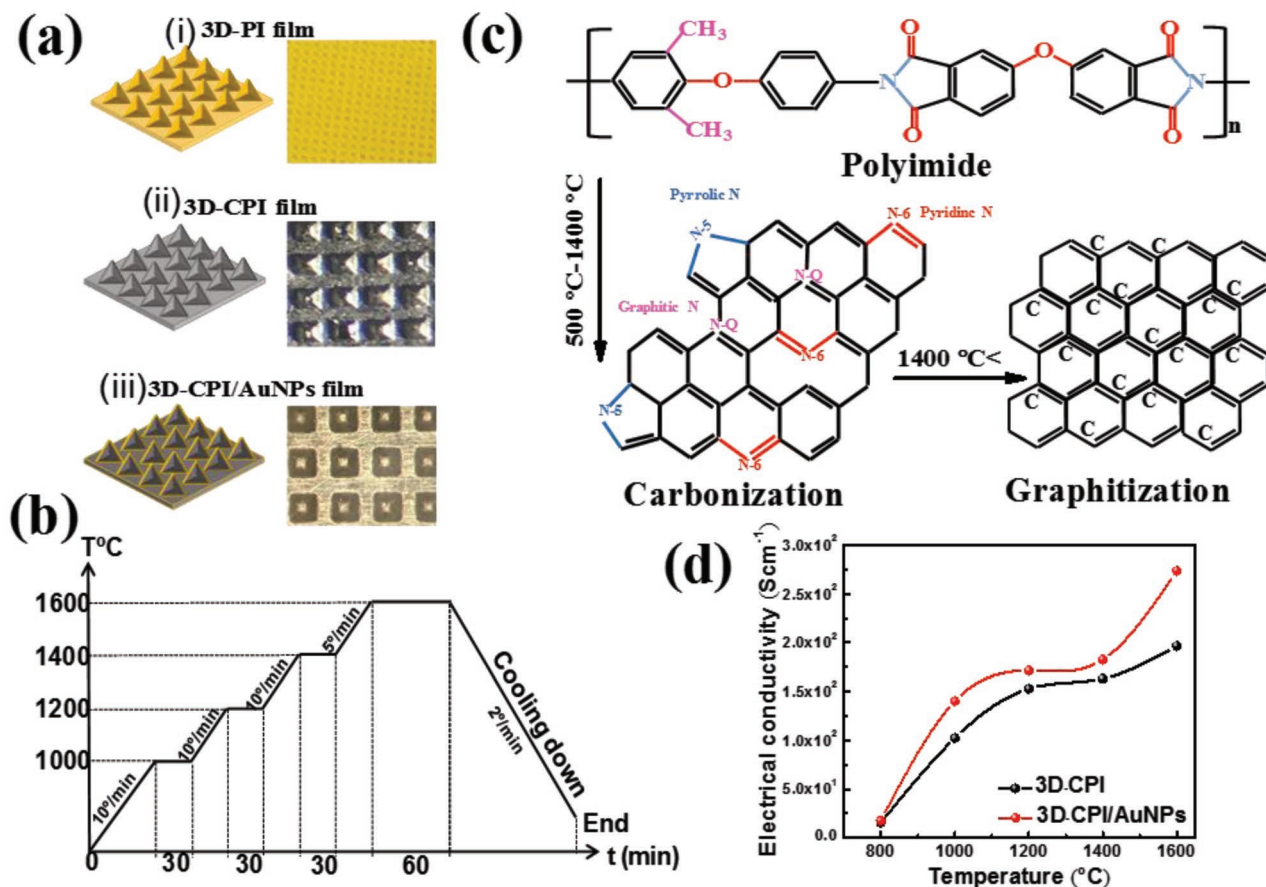


**Figure 1.** a) Schematic illustration of the 3D microstructured FSS i) PI film (Scale: 150 μm), ii) CPI film (Scale: 100 μm), iii) CPI/AuNPs film (scale: 100 μm). b) Temperature profile of carbonization was performed in the vacuum tube furnace (GLS-1800X). c) Mechanism involved in carbonization of microstructured polyimide film with temperature. d) Electrical conductivity of 3D-CPI films and 3D-CPI/AuNPs films at different carbonization temperatures (800, 1000, 1200, 1400, and 1600 °C).

the insulating polyimide film through the process of carbonization and graphitization, as shown in Figure 1b. The mechanism involved in the conversion of pristine 3D microstructured polyimide film into a metallic 3D carbonized polyimide film is shown in Figure 1c, where the polyimide (PI) film consists of imide monomers undergoes the processes of dehydrogenation, deoxygenation, denitrogenation, carbonization, and graphitization. To fabricate the pristine 3D microstructured polyimide film into 3D graphitic carbon microstructured film, a sequential time-controlled temperature profile of 800, 1000, 1200, 1400, and 1600 °C was optimized. The carbonization temperature-dependent electrical conductivity of 3D-CPI film and 3D-CPI/AuNPs film was used to estimate the efficiency of the carbonization/graphitization process as shown in Figure 1d, where the electrical conductivity rises with increasing temperature. Also, the gold deposited 3D-CPI/AuNPs film shows a higher electrical conductivity than 3D-CPI film all over the temperature range.

The conductivity of pristine PI film is known to be insulating under ambient conditions, the carbonization process from 800 to 1600 °C causes a rise in the conductivity from the order of  $10^1$  to  $10^2$  S  $\text{cm}^{-1}$ . Additionally, the deposition of AuNPs onto 3D CPI film causes a further rise in their electrical conductivity, as shown in Table S1 (Supporting Information). The carbonization and graphitization processes show that the graphitized film possesses a higher crystalline orientation of repeating units, leading to higher electrical conductivity and mobility. Furthermore,

increasing  $\text{sp}^2$  carbon atoms (pi bonds) at higher temperatures creates a monocyclic carbon ring, which increases the free-electron mobility in the carbon ring without any barriers and simultaneously improves electronic conductivity in agreement with the results of FTIR and XPS in the below discussion.<sup>[20–22]</sup>

The fabricated 3D pyramidal microstructured CPI and CPI/AuNPs FSS films were characterized by scanning electron microscopy (SEM) and the elemental distribution of carbon and gold elements was analyzed by energy dispersive X-ray as shown in Figure 2a. The Raman spectra were obtained using the Raman Spectrometer to characterize the electron–phonon interaction and ascertain the  $\text{sp}^3$ ,  $\text{sp}^2$ - hybridization using an excitation laser wavelength of 514 nm. Figure 2b shows the Raman spectroscopy of 3D microstructured FSS CPI films at different carbonization temperatures profiles, exhibiting a weak D-band at 1350  $\text{cm}^{-1}$  arising from a defect in the  $\text{sp}^2$  carbon structure. The weak G-band at around 1580  $\text{cm}^{-1}$  is formed by the stretching C–C bond in graphitic materials, which is common in all  $\text{sp}^2$ -hybridization carbon types. The 2D band around 2750  $\text{cm}^{-1}$  is the second-order scattering of the D band. The intensity ratio from the 2D-band to the G-band ( $I_{2D}/I_G$ ) is associated with the graphene layer. The peak intensity ratio of  $I_D/I_G$  can determine the disorder of the degree of graphitization corresponding to the proportion of  $\text{sp}^3$ -hybridized carbon atoms in  $\text{sp}^2$  conjugated carbon structures. However, the intensity ratio of  $I_D/I_G$  decreases with the increasing amount of ordered graphitic carbon, and we note that the higher

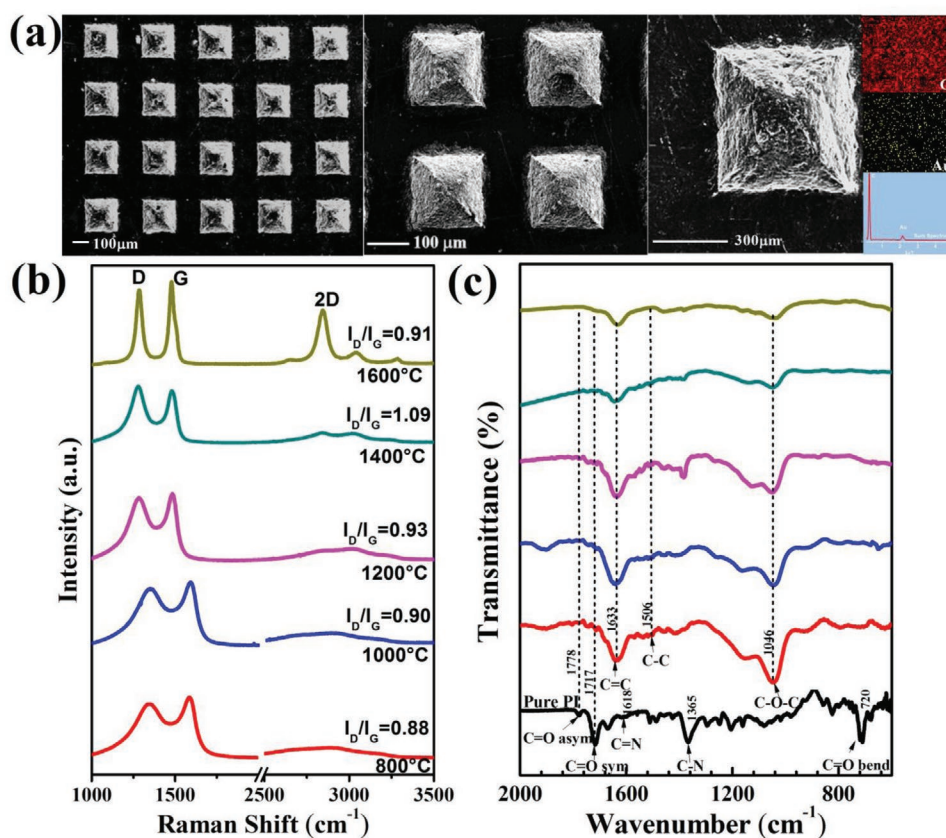


**Figure 2.** a) SEM images of 3D-CPI/AuNPs FSS film. b) Raman spectra and c) FT-IR spectra of 3D-CPI FSS films at different carbonized temperatures (800, 1000, 1200, 1400, and 1600 °C).

temperature can cause more defects in the  $sp^2$  carbon than at lower temperatures.<sup>[23]</sup>

Our results show that the intensity ratio of  $I_D/I_G$  increases with increasing temperature (0.88, 0.90, 0.93, 1.09, and 0.91) due to the increasing defects and crystallinity from thermal treatment. The crystalline size ( $L_a$ ) is determined by first-order Raman scattering using the formula:

$$\frac{I_D}{I_G} = \frac{C(\lambda)}{L_a} \quad (1)$$

where  $L_a$  is the in-plane crystallite size,  $C$  ( $2.4 \times 10^{-10} \lambda^4$ ) is a fitting constant,  $\lambda$  is the wavelength of the laser source (514 nm) and  $I_D/I_G$  is the intensity ratio between D and G bands.<sup>[24]</sup> The crystallite size  $L_a$  (19.0, 18.6, 18.0, 15.4, and 18.4) is gradually smaller with increasing temperature (800–1600 °C). Considering  $L_a$  as an average inter-defect distance, we can assume that the higher the number of defects, the higher the D peak intensity that can cause the smaller  $L_a$ . The FTIR and XPS results support the fact that it assists dehydrogenation, deoxygenation, and denitrogenation and improves  $sp^2$  hybridization.<sup>[25]</sup> The chemical structures of 3D microstructured FSS carbonized PI films at 800, 1000, 1200, 1400, and 1600 °C were measured by FT-IR spectroscopy as shown in Figure 2c. The peaks at 720, 1365, 1778, and 1717  $cm^{-1}$  observed in pure polyimide film, correspond to C=O bending during the formation of the imide ring during the preparation of PI, C–N stretching, C=O asymmetric stretching, and symmetric stretching, respectively. In addition, the peak at 1618  $cm^{-1}$  is identified to be C=N (carbonyl) groups, and the peak at 1046  $cm^{-1}$  is attributed to C–O–C stretching vibrations of the C–O groups. The absorption bands arising at 1633  $cm^{-1}$  and 1506  $cm^{-1}$  are assigned to the C=C and C–C stretching vibrations of the aromatic ring. The C=O bending the formation of imide ring, C=O (symmetric and asymmetric stretching), the amines C=N and C–N, gradually disappear due to the dehydrogenation, deoxygenation, and denitrogenation with increasing temperature.<sup>[26,27]</sup>

The surface composition of 3D microstructured CPI FSS film was studied with the XPS technique using Al  $K\alpha$  radiation ( $h\nu = 1486.7$  eV), pass energy of 143.05 eV for survey spectra. An overview of XPS spectra of 3D microstructured FSS carbonized PI films at 800, 1000, 1200, 1400, and 1600 °C are displayed in Figure 3a. The surveyed spectra consist of C1s, O1s, and N1s, which represent the final composition of the sample. In the surveyed spectra, the nitrogen content decreases with the increasing temperature order of 800–1600 °C. Figure 3b shows the deconvolution of O1s XPS spectra of 3D microstructured FSS CPI films at 800, 1000, 1200, 1400, and 1600 °C, respectively.

The oxygen double-bonded to the aromatic carbon, C=O denotes peak I with a binding energy of  $530.7 \pm 0.2$  eV, the deconvoluted O1s peak II represents the O–(C=O\*)–C (aromatic) corresponding to the binding energy  $531.8 \pm 0.3$  eV and O–C–O or C–O–C (aromatic) denotes peak III corresponding to the binding energy of  $532 \pm 1$  eV at different carbonization temperatures 800, 1000, 1200, 1400, and 1600 °C, respectively.<sup>[28–30]</sup> The deconvolution of N1s XPS spectra of 3D microstructured FSS CPI films at different carbonization temperatures of 800, 1000, and 1200 °C is shown in Figure 3c. The nitrogen bonds are not observed for the carbonization at 1400 and 1600 °C unless the detected small signal of nitrogen bonds

overlaps with the noise signals (Figure S1, Supporting Information). The N1s peaks are divided into three main components (pyridinic, N-6), (pyrrolic/pyridine, N-5), and (quaternary, N-Q). The de-convoluted N1s peaks at  $398 \pm 0.3$  eV (16.56%),  $400.14 \pm 0.6$  eV (59.76%) and  $401.1 \pm 0.5$  eV (23.71%) can be attributed to (pyridinic, N-6), (pyrrolic/pyridine, N-5), and (quaternary, N-Q) at carbonization temperatures 800, 1000, and 1200 °C shown in Figure 3c.<sup>[28,29]</sup> The high-resolution core level of C1s XPS spectra of 3D microstructured FSS CPI films at carbonization temperatures of 800, 1000, 1200, 1400, and 1600 °C are shown in Figure 3d. The curve fitting was obtained with Gaussian lines. The  $sp^2$ -bonded functional group, C=C corresponds to the binding energy of 284.3 eV, (the  $sp^3$ -bonded function group, C–C corresponds to the binding energy of  $284.8 \pm 0.2$  eV, the carbonyl carbon groups C–O, C=O corresponds to binding energy of  $286 \pm 1$  and  $289.6 \pm 1$  eV at carbonization temperatures of 800, 1000, 1200, 1400, and 1600 °C. N- $sp^2$  bond, C–N corresponds to the binding energy of  $285.7 \pm 0.1$  eV at carbonization temperatures of 800, 1000, and 1200 °C. N- $sp^3$  bond, C=N corresponds to the binding energy of  $287.7 \pm 0.8$  eV (2.54%) at carbonization temperatures 800, 1000, 1200, and 1400 °C. However, N- $sp^2$  bond, C–N cannot be detected at the carbonization temperature 1400 and 1600 °C, N- $sp^3$  bond, C=N can be found at 1400 °C. From the de-convoluted C1s analysis, the C=C carbon peak is narrower and sharper than at 1600 °C, which indicates that the sample has high crystallinity.<sup>[33–35]</sup>

The quantitative atomic percentage (at.%) of C1s, O1s, and N1s derived from XPS results is shown in Figure 4a. The rate of carbon content increases as a function of carbonization temperature, as indicated by the gradual decrease of O/C surface composition from 0.067 to 0.022 as a function of the temperature.

Similarly, the atomic ratio N/C dramatically decreases from 0.013 to 0.001. The atomic ratio O/C = 0.022 and N/C = 0.001 at 1600 °C indicate that the complete carbonization process correlates with the temperature, in other words, the carbon signal increases with temperature as shown in Figure 4b. The carbon atoms from the broken graphitic sheet are replaced by the nitrogen signal, which reduces with increasing temperature.<sup>[33,36]</sup> The atomic percentage of the C=C carbon increases by forming a graphite-like structure as a function of temperature. The  $sp^2$  hybridized carbon dramatically increases, as highlighted by Raman and FTIR results. The other carbon functional groups steadily change with increasing temperature. C=N groups show up to carbonization temperature 1400 °C and C–N does not exist at both 1400 and 1600 °C. However, there are no nitrogen bonds at 1600 °C that can leave residual graphitic nitrogen at 1400 °C shown in Figure 4c.<sup>[37,38]</sup> The atomic percentage carbonyl group C=O (I) and O–C–O or C–O–C (II) from aromatic ring slightly increases when attached on graphitic carbon layer after graphitization with increasing temperature as shown in Figure 4d. The atomic percentage of O–(C=O\*)–C (III) hydrocarbon from the aliphatic/aromatic ring dramatically decreases as a function of temperature. The atomic percentage of the N1s components is shown in Figure 4e. The atomic percentage of pyridinic, N-6 atom slightly increases with increasing temperature which seems that pyridinic, N-6 atom is substituted on the six-membered ring at the edge of the graphitic carbon layer. The atomic percentage of pyrrolic/pyridine N-5 atom is higher at 800 and 1600 °C

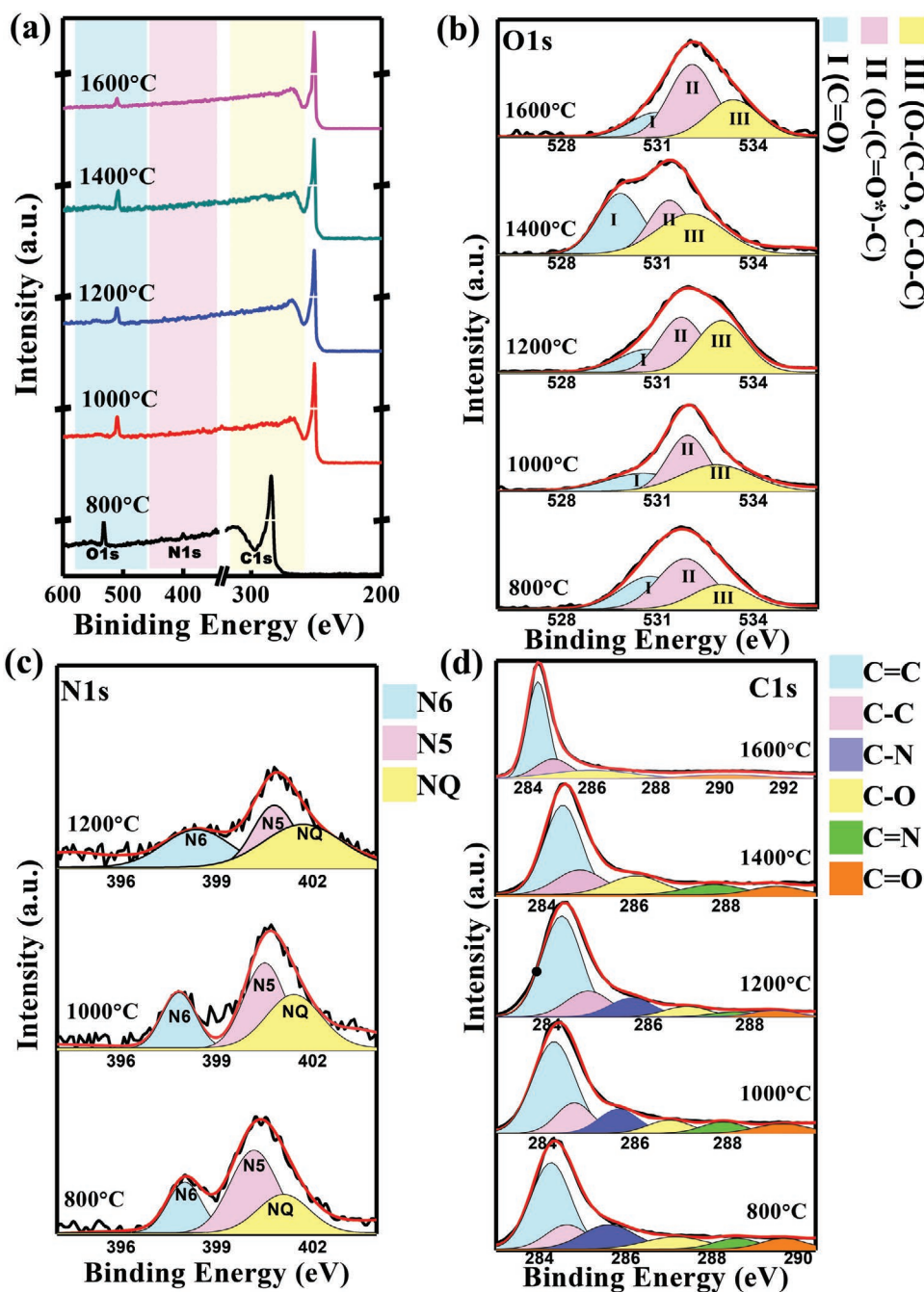


**Figure 3.** a) XPS survey spectra of 3D-CPI FSS films. b) The deconvolution of O1s XPS spectra. c) The deconvolution of N1s XPS spectra. d) High-resolution core level of C1s XPS spectra at different carbonization temperature (800, 1000, 1200, 1400, and 1600 °C).

than at 1000 °C. On the other hand, the atomic percentage of graphitic N-Q atoms is highest at 1000 °C, which occupies the place of the carbon atom. The electronic conductivity is conserved at 1000 °C, considering the number of substituted graphitic N-Q increases while the graphitic benzene ring increases at high temperatures. The pyrrolic/pyridine N-5 connects with two  $sp^2$  carbon neighbors, and both N-6 and N-5 atoms produce a pair of valence electrons and create vacancies in the graphitic carbon layer. The vacancies allow a free electron diffusion to improve the electronic conductivity shown in Figure 4f.<sup>[24]</sup> The

detail of each component binding energy and percentage of C1, O1s, and N1s are described in Table S2 (Supporting Information). The plasmon loss spectra and the  $\pi$  bond shake-up satellite were observed for C1s XPS spectra of 3D microstructured FSS carbonized PI films at carbonization temperature 800, 1000, 1200, 1400, and 1600 °C (Figure S2, Supporting Information). The plasmon loss feature is related to the photoelectron loss of energy due to inelastic scattering with the valence electrons of the material. The bulk plasmon loss peaks occur around 28.2 eV at 800, 1000, 1200, and 1600 °C, while the bulk

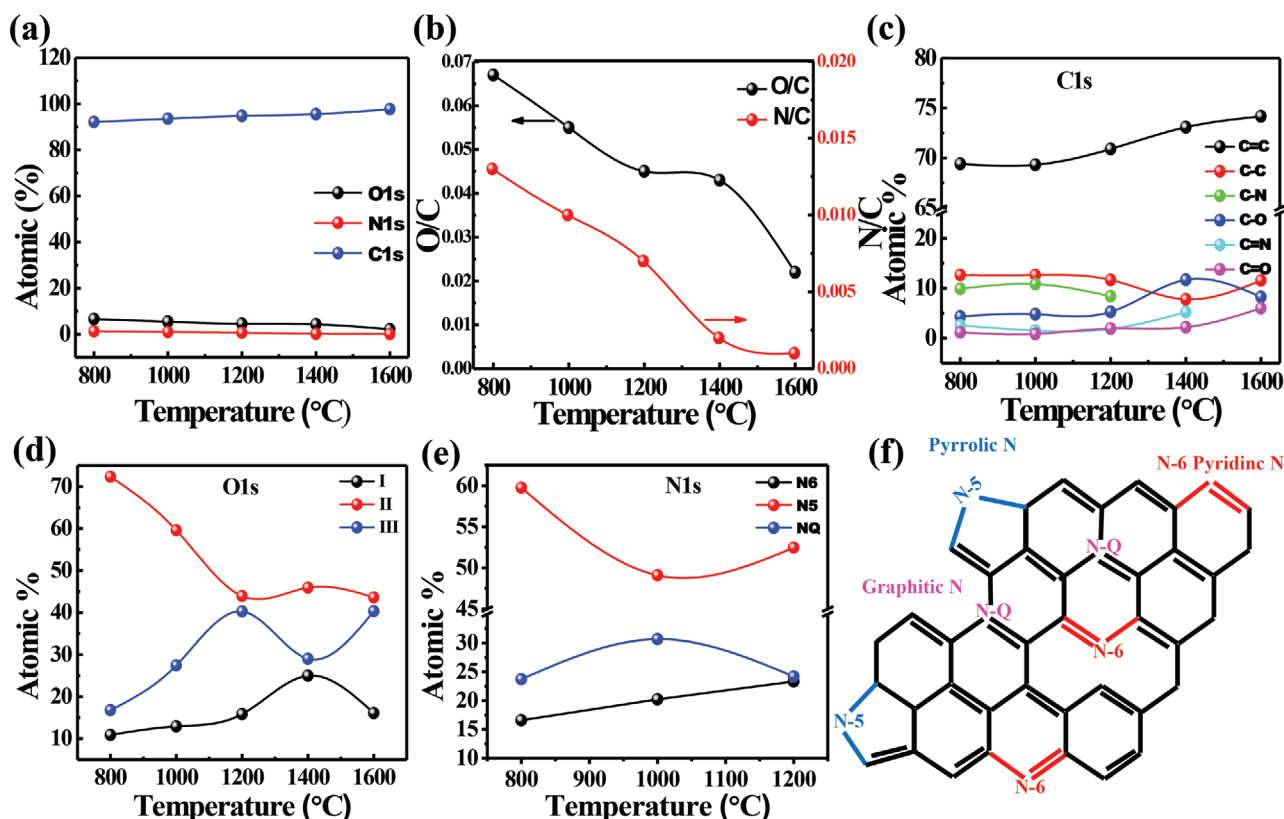


**Figure 4.** a) The atomic percentage of O1s, N1s, and C1s. b) The atomic ratio of O/C and N/C at different temperatures (800, 1000, 1200, 1400, and 1600 °C). c–e) The atomic percentage of functional components groups of C1s (c), O1s (d) and N1s (e) as function of temperature. f) Schematic diagram of nitrogen atoms occupied at the graphitic sheet.

plasmon loss peaks shift around 25.4 eV at 1400 °C from C1s core level (284.3 eV). The  $\pi \rightarrow \pi^*$  satellite presents at higher binding energy 6.4 eV from the core level of C1s. The presence of the  $\pi \rightarrow \pi^*$  satellite indicates that the extended delocalized electrons from the  $sp^2$  photoexcitation carbon. The  $\pi$  bond arises with increasing temperature that is associated with the  $\pi$  bond in graphite-like carbon.<sup>[39,40]</sup>

The valence band maximum  $E_{VBM}$  1.52, 15.7, 1.59, 1.5, and 2.5 eV are obtained from the valence band spectra and energy bandgap  $E_g$  between the conduction band minimum and the valence band maximum is 14, 14.9, 15, 14.8, and 15.5 eV are obtained from C1s XPS spectra at different temperatures as shown in Figure 5a–e. The illustration of the energy level diagram of C1s carbon is as shown in Figure 5f. The energy ( $E_{C1s} - E_{VBM}$ ) different from the core level of C1s is 282.78, 282.73, 282.72, 282.8, and 281.8 eV. The valence band maximum  $E_{VBM}$  shifts from the Fermi level (zero binding energy) with increasing temperature, while the conduction band minimum  $E_{CBM}$  shifts toward the valence band maximum  $E_{VBM}$ . The formation energy shift with increasing temperature induces band bending and causes the exponential band tail to have binding energy due to the high conductivity of the graphitic  $sp^2$  carbon.<sup>[41,42]</sup>

Having fabricated the metallic 3D microstructured CPI films possessing high conductivity, we investigate their resonance frequency and characterize their terahertz frequency selective surface performance using THz time-domain spectroscopy. The

as-measured THz reflectance of “planar” CPI and CPI/AuNPs films set and “3D microstructured” carbonized PI and PI/AuNPs films set are shown in Figure 6a,b. From the reflectance spectra, we can depict that the frequency response of 3D microstructured CPI films dominates over the frequency response of planar CPI films with and without AuNPs. Further to understand the frequency-selective surface properties of the 3D microstructured CPI films, we analyze the critical parameters like voltage standing wave ratio (VSWR), reflection coefficient, and return loss required for an effective terahertz frequency selective surface. VSWR is the ratio of the maximum to minimum voltage standing wave pattern and is a measure of how much signal is reflected from the antenna to the source. The reflection coefficient  $|\Gamma|$  indicates how much of an EM wave is reflected by an impedance of the load;  $|\Gamma|$  is the ratio of the power incident on the load to power reflected on the source, also known as  $|S_{11}|$ . The return loss measures the amount of power delivered from a transmission line to the load, not reflected as a reflection to the source. Larger values of return loss mean better matching of the load and line impedance. It is expressed in dB and a positive quantity of reflected power is less than incident power. Return loss RL (in dB) is defined as

$$RL = 10 \log \left[ \frac{P_{in}}{P_{ref}} \right] \text{ dB} \quad (2)$$

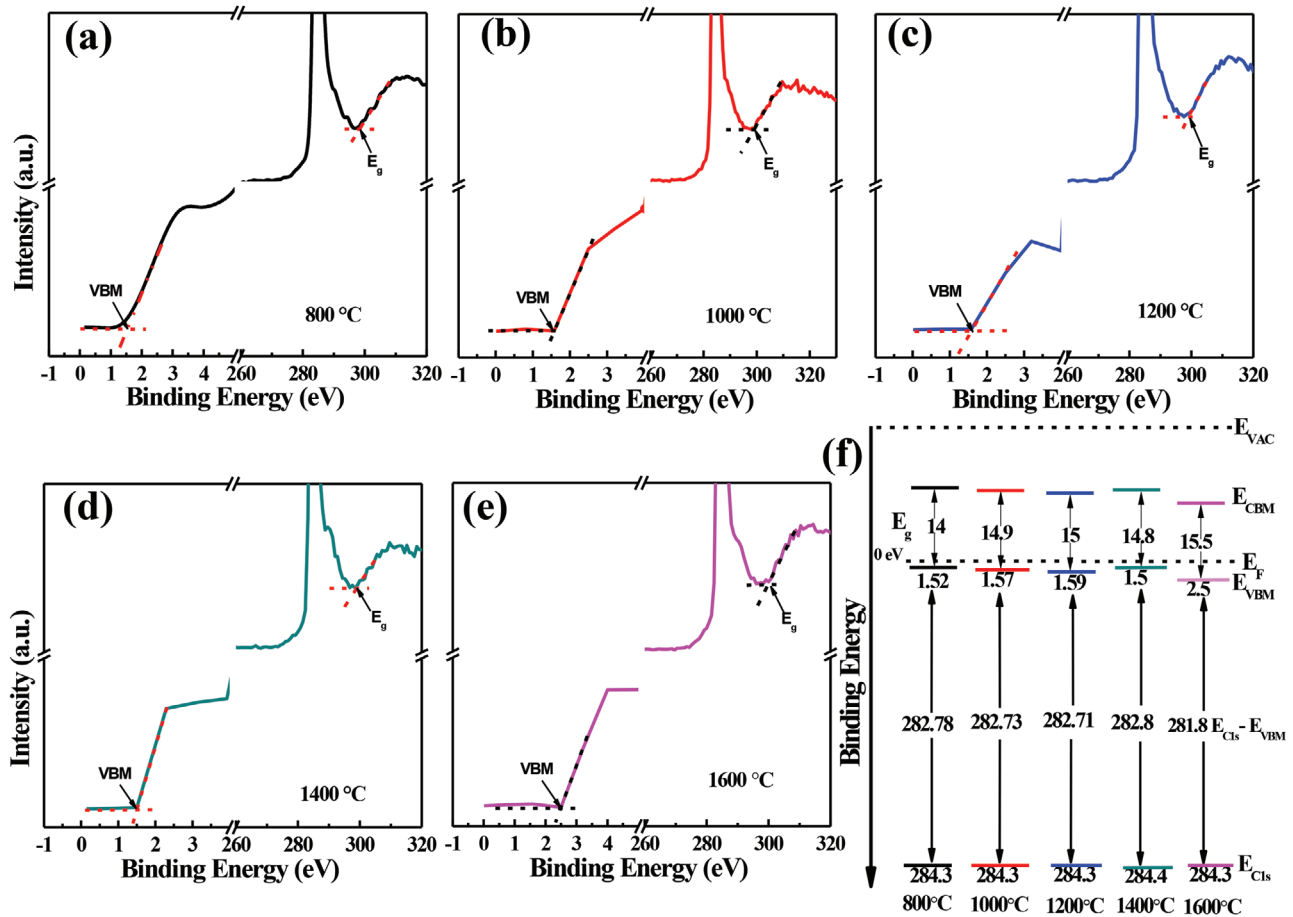


**Figure 5.** Valence band maximum and energy gap spectra of 3D-CPI FSS films and CPI/AuNPs films at a) 800 °C, b) 1000 °C, c) 1200 °C, d) 1400 °C, e) 1600 °C. f) Energy levels of C1s as a function of different temperatures.

where RL is expressed as a power in terms of voltage in a transmission line or waveguide. Return loss is the negative of the reflection coefficient  $|\Gamma|$ :

$$RL = 10 \log \left[ \frac{1}{|\Gamma|^2} \right] \text{dB} \quad (3)$$

$$= -20 \log [|\Gamma|] \text{dB} \quad (4)$$

where  $\Gamma$  is the complex reflection coefficient at the input of the source. Return loss is expressed in terms of voltage standing wave ratio, VSWR, in Equation (5):<sup>[43,44]</sup>

$$RL = -20 \log \left[ \frac{\text{VSWR} - 1}{\text{VSWR} + 1} \right] \text{dB} \quad (5)$$

where  $\text{VSWR} = \left[ \frac{1+|\Gamma|}{1-|\Gamma|} \right]$  and  $|\Gamma| = \left[ \frac{\text{VSWR} - 1}{\text{VSWR} + 1} \right]$ . The return loss RL of planar and 3D microstructured FSS CPI and those of AuNPs modified films were measured at scan range between 0.1 and 3.5 THz and the responsible frequency performed between 0.5 and 1.5 THz. The return loss of CPI-planar and CPI/AuNPs-planar films exhibits 22.4 dB and 24.6 dB at the resonance frequency of 1.1 THz, as shown in Figure 6c. 3D

microstructured FSS CPI and CPI/AuNPs modified films resonate at 1 and 1.06 THz and have the return loss of 40.5 dB and 43.7 dB, demonstrating the resonance frequencies as shown in Figure 6d. Since both CPI/AuNPs-planar and 3D microstructured FSS CPI/AuNPs films have a higher return loss than those of non-modified AuNPs films, this shows that the films seem to be affected by the plasmonic effect. 3D microstructured CPI/AuNPs FSS film owing to the plasmonic effect where the EM wave interacts with the metal nanoparticles induces the oscillation of the conducting electrons. The frequency of the oscillation electrons coherent with the frequency of the delocalized electrons by scattered or reflected radiation at the internal surfaces of the carbon materials can cause the strong plasmon resonance frequency. The resonance frequency of 3D-CPI/AuNPs results in blueshift due to plasmonic oscillation of each AuNPs interaction with the scattering neighboring AuNPs.<sup>[45–48]</sup>

However, the return loss of CPI-planar and CPI/AuNPs-planar films is low when compared with the 3D microstructured FSS CPI and CPI/AuNPs films. This is because the high reflection coefficient from the load to the source and their plasmonic frequency on 3D microstructured CPI/AuNPs interacts with the reflected frequency from the load to the source making up the higher resonance frequency and return loss.<sup>[49,50]</sup> Meanwhile, as both 3D microstructured CPI and CPI/AuNPs films

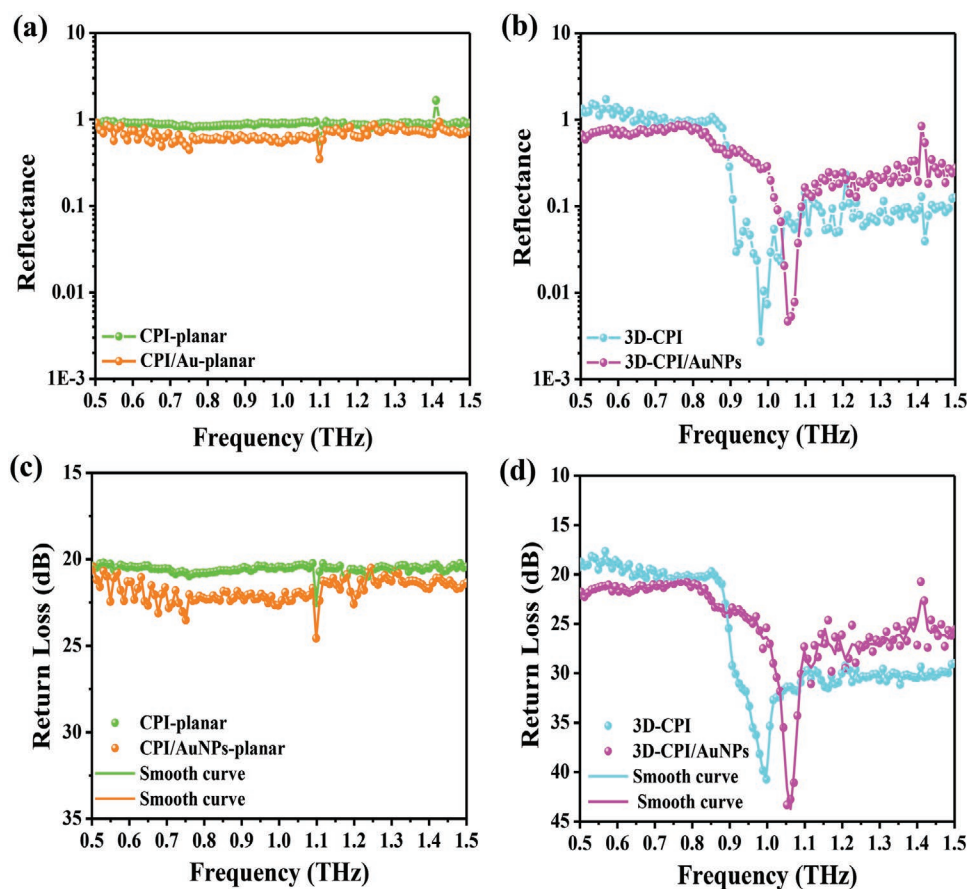


**Figure 6.** Reflectance as-measured semi-log graph of a) planar CPI and CPI/AuNPs films and b) 3D-CPI and 3D-CPI/AuNPs FSS films. Return loss of c) planar CPI and CPI/AuNPs films and d) 3D-CPI and 3D-CPI/AuNPs FSS films.

demonstrate a high return loss and distinct excitation resonance frequencies. There are three main mechanisms for EMI shielding materials such as reflection, absorption, and multiple reflections. According to the transmission line or waveguide, the more significant return loss represents the amplitude of the reflected wave that reduces the incident wave. In other words, the reflected radiation from the load to the source is less than the radiation absorbed by the load. That means the return loss has expressed the value opposite to the reflectance. 3D microstructured CPI and CPI/AuNPs FSS films have higher mobile charge carriers that interact with the electromagnetic radiation that produces lower reflectance for EMI shielding than CPI-planar and CPI/AuNPs-planar films. Therefore, the return loss

**Table 1.** Skin depth of CPI-planar, CPI/AuNPs-planar and 3D-CPI and 3D-CPI/AuNPs films.

Samples	Conductivity [S cm <sup>-1</sup> ]	Frequency [THz]	Skin depth [μm]	Thickness of sample [μm]
CPI-planar	51.18	1.1	6.7	≈30
CPI/AuNPs-planar	55.17	1.1	6.4	≈30
3D-CPI	196.57	1	3.5	≈80
3D-CPI/AuNPs	273.54	1.06	2.9	≈80

of 3D microstructured CPI and CPI/AuNPs FSS films increases with a strong excitation resonance frequency compared to CPI-planar and CPI/AuNPs-planar films. The return loss induces the secondary mechanism as absorption for EMI shielding by interacting the electric or magnetic dipoles of the materials with the electromagnetic radiation. Absorption and return loss can be described according to the relation between absorption coefficient, reflection, and transmission that is expressed by the formula:  $A = 1 - R - T$ . As FSS carbon-based materials are semi-metallic materials, the transmission tends to almost zero. Therefore, the maximum value of absorption indicates the minimum value of reflectance/the maximum value of return loss.<sup>[51–54]</sup> The latter mechanism is multiple reflections, which are the internal reflections between the interfaces of the shielding material. Significantly, multiple reflections reduce the overall shielding value if the material thickness is thinner than the skin depth, since 3D microstructured CPI and CPI/AuNPs FSS films have large internal surfaces as foam. The skin depth is the depth of the conductor at which the strength of the electric field drops to (1/e) of the incident strength:

$$\delta = \frac{1}{\sqrt{\pi f \mu \sigma}} \quad (6)$$

where  $\delta$  is the skin depth,  $f$  is the frequency,  $\mu$  is the magnetic permeability ( $\mu = \mu_0 \mu_r$ ),  $\mu_0 = 4\pi \times 10^{-7}$  H m<sup>-1</sup>, for graphite,



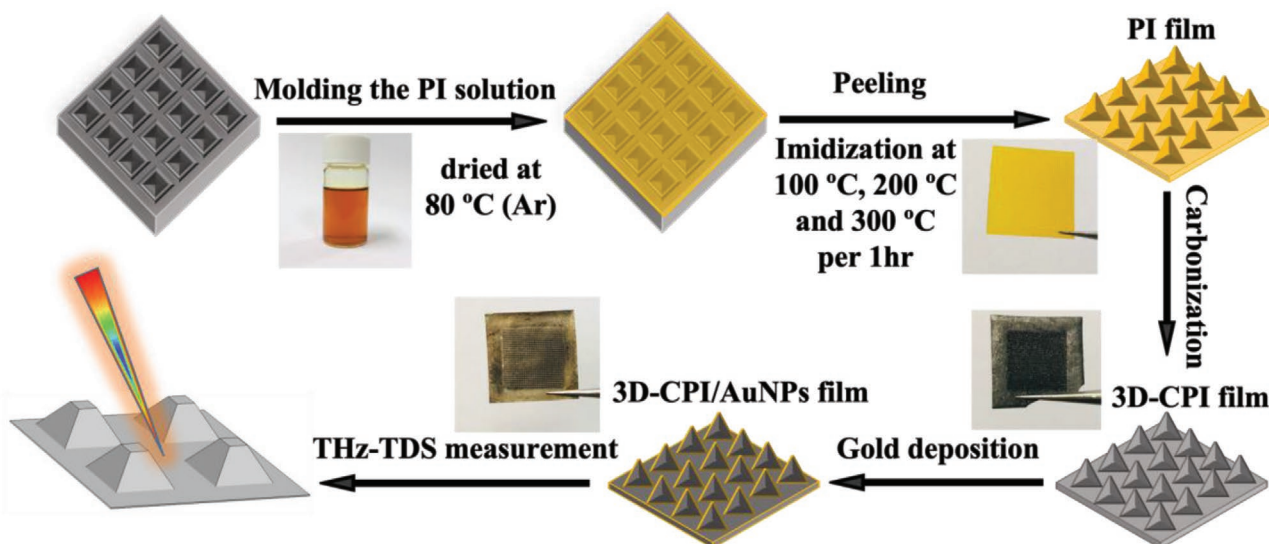


**Figure 7.** The schematic diagram of the sample preparation of 3D-CPI and 3D-CPI/AuNPs films.

$\mu_r \approx 1$ , relative magnetic permeability, and  $\sigma$  is the electrical conductivity of the material. The skin depth of 3D microstructured CPI and CPI/AuNPs FSS films can be neglected due to their higher thickness (Table 1). As the comparison of CPI-planar and 3D microstructured CPI, 3D-CPI obviously impacts the secondary and the third mechanisms for the EMI shielding.<sup>[55–57]</sup> Therefore, a 3D microstructured CPI FSS structure has a high potential to be used as an EMI shielding material owing to the main mechanisms of shielding properties.

### 3. Conclusions

3D microstructured CPI and 3D-CPI/AuNPs FSS films were systematically fabricated with carbonization/graphitization enhanced mechanical and electrical properties by carbonization/graphitization under different temperatures. Our study demonstrated that the graphitized films possess a higher crystallite orientation of repeating units, leading to higher conductivity. The 3D microstructured CPI and 3D-CPI/AuNPs FSS films show a higher return loss with the distinct resonance frequency of CPI-planar and CPI/AuNPs films. 3D-CPI/AuNPs film exhibits a larger value of return loss and a stronger resonance frequency owing to the plasmonic interaction with the incident EM wave that induces the mechanism for EMI shielding. Therefore, we demonstrate the efficient processing, structuring, and capability of carbon materials for terahertz applications.

### 4. Experimental Section

The organo-soluble polyimide (PI) with a solid content of 1.5 wt.% was completely dissolved in DMF and continuously stirred at room temperature for over 12 h.<sup>[58,59]</sup> The transparent yellow PI solution was poured into the microstructured mold and immediately put in a vacuum oven to pump the bubbles from the solution repeatedly. The entire process of the sample preparation is illustrated in detail in Figure 7. The PI solution was dried at 80 °C to evaporate the DMF solvent under

the inert gas environment. The microstructured PI film was obtained by peeling off from the mold, followed by the thermal imidization process that is a functional process for achieving any desired shape. The microstructured PI film was annealed under 100, 200, and 300 °C for 1 h at each temperature in the vacuum furnace to remove residual molecules from the solvent.<sup>[60–62]</sup>

The microstructured PI film was sandwiched between carbonization molds and placed into a tube furnace under argon gas flow for pre-carbonization using a temperature profile from 200 to 1000 °C as shown in Figure S3 (Supporting Information). Further, the microstructured carbonized PI films were sandwiched between supporting graphite plates and using the vacuum tube furnace (GLS-1800X) high-temperature graphitization was carried out by gradually increasing temperature to 1000, 1200, and 1400 °C with a heating rate of 10 °C min<sup>-1</sup> and stabilized at 1600 °C with a heating rate of 5 °C min<sup>-1</sup> for 1 h, under an argon flow rate of 10 L min<sup>-1</sup>. The final thickness of a pyramid of 3D-CPI obtained was  $\approx 80 \mu\text{m}$  (Figure S4, Supporting Information). After carbonization, 15 nm of the gold layer was deposited on the 3D-CPI film and consequently given heat treatment at 400 °C for 1 h to obtain 75–100 nm diameter AuNPs<sup>[63–65]</sup> which were characterized by field emission SEM (FE-SEM, QUANTA FEG250, USA) (Figure S5, Supporting Information). Fourier transformation infrared (FT-IR) spectrometry (Nicolet Avatar-360) and X-ray photoelectron spectroscopy (XPS, PHI-5400, Physical Electronics) were performed to investigate the 3D-CPI films. Raman spectroscopy and Hall effect measurement system (ECOPIA, HMS-5300) were used to measure carbon products, especially considering conjugated and double carbon–carbon bonds lead to high Raman intensities and the electrical conductivity of 3D-CPI and 3D-CPI/AuNPs films, respectively. These films were characterized by SEM (FEI Quanta 200FEG, USA) and energy dispersive elemental mapping. The optical properties of the films were ascertained by THz time-domain spectroscopy (THz-TDS, TOPTICA Photonics) THz-TDS, TOPTICA Photonics developed femtosecond laser with the widest range maximum of 3.5 THz (116 cm<sup>-1</sup>) that has better spectral resolution than 2.5 GHz (0.08 cm<sup>-1</sup>). The real-time data acquisition 10 spectra s<sup>-1</sup> could swiftly yield information about the transmission and reflection modes.

### Supporting Information

Supporting Information is available from the Wiley Online Library or from the author.

## Acknowledgements

This work was supported by the RGC of Hong Kong SAR project number T42-103/16N.

## Conflict of Interest

The authors declare no conflict of interest.

## Data Availability Statement

The data that supports the findings of this study are available from the corresponding author upon reasonable request.

## Keywords

band stop filter, carbon materials, EMI shielding, frequency selective surface, terahertz spectroscopy

Received: October 11, 2021

Revised: January 9, 2022

Published online: March 2, 2022

- [1] M. H. Nisanci, A. Y. Tesneli, N. B. Tesneli, B. Colak, F. De Paulis, A. Orlandi, *IEEE Trans. Electromagnet. Compat.* **2018**, 1.
- [2] J. Wang, S. Qu, L. Li, J. Wang, M. Feng, H. Ma, H. Du, Z. Xu, *J. Adv. Dielectr.* **2017**, 7, 27.
- [3] R. R. Hartmann, J. Kono, M. E. Portnoi, *Nanotechnology* **2014**, 25, 322001.
- [4] H. Liang, J. Liu, Y. Zhang, L. Luo, H. Wu, *Composites, Part B* **2019**, 178, 107507.
- [5] H. Liang, H. Xing, Z. Ma, H. Wu, *Carbon* **2021**, 183, 138.
- [6] X. Xu, K. Chuang, R. J. Nicholas, M. B. Johnston, L. M. Herz, *J. Phys. Chem. C* **2009**, 113, 18106.
- [7] S. Kumar, N. Kamaraju, B. Karthikeyan, M. Tondusson, E. Freysz, A. K. Sood, *J. Phys. Chem. C* **2010**, 114, 12446.
- [8] P. Tassin, T. Koschny, C. M. Soukoulis, *Science* **2013**, 341, 620.
- [9] O. V. Kibis, *Journal of Nanophotonics* **2010**, 4, 040102.
- [10] G. Chen, R. Shrestha, A. Amori, Z. Staniszewski, A. Jukna, A. Korliov, C. Richter, M. El Fray, T. Krauss, R. Sobolewski, *J. Phys.: Conf. Ser.* **2017**, 906, 012002.
- [11] C. J. Docherty, M. B. Johnston, *Journal of Infrared, Millimeter, and Terahertz Waves* **2012**, 33, 797.
- [12] H. S. Lee, J. ho Park, J. K. Singh, H. J. Choi, S. Mandal, J. M. Jang, H. M. Yang, *Materials* **2020**, 13, 895.
- [13] H. Liang, H. Xing, M. Qin, H. Wu, *Composites, Part A* **2020**, 135, 105959.
- [14] Q. Huang, G. Wang, M. Zhou, J. Zheng, S. Tang, G. Ji, *J. Mater. Sci. Technol.* **2022**, 108, 90.
- [15] R. Mi, W. Zhang, K. Ghosh, S. Walunj, Q. Liu, J. Rollin, P. Sochoux, D. Pommerenke, V. Khilkevich, in *2021 IEEE International Joint EMC/SI/PI and EMC Europe Symposium*, **2021**, pp. 266.
- [16] R. Jaiswar, F. Mederos-Henry, V. Dupont, S. Hermans, J.-P. Raskin, I. Huynen, *J. Mater. Sci.: Mater. Electron.* **2020**, 31, 2190.
- [17] M. Inagaki, N. Ohta, Y. Hishiyama, *Carbon* **2013**, 61, 1.
- [18] S. Venkatachalam, D. Bertin, G. Ducournau, J. F. Lampin, D. Hourlier, *Carbon* **2016**, 100, 158.
- [19] H. Zhang, J. Horvat, R. A. Lewis, in *2016 41st International Conference on Infrared, Millimeter, and Terahertz Waves (IRMMW-THz)*, **2016**, <https://doi.org/10.1109/IRMMW-THz.2016.7758466>.
- [20] N. Deprez, D. S. McLachlan, *J. Phys. D: Appl. Phys.* **1988**, 21, 101.
- [21] G. Tian, H. Zhang, J. liu, S. Qi, D. Wu, *Polymer Science Series A* **2014**, 56, 505.
- [22] P. Zhang, *J. Mater. Sci.: Mater. Electron.* **2017**, 28, 14515.
- [23] O. A. Maslova, M. R. Ammar, G. Guimbreti, J. Rouzaud, P. Simon, *Phys. Rev. B.* **2012**, 86, 134205.
- [24] N. C. Abeykoon, V. Garcia, R. A. Jayawickramage, W. Perera, J. Cure, Y. J. Chabal, K. J. Balkus, J. P. Ferraris, *RSC Adv.* **2017**, 7, 20947.
- [25] A. C. Ferrari, *Solid State Commun.* **2007**, 143, 47.
- [26] L. Bin Zhang, J. Q. Wang, H. G. Wang, Y. Xu, Z. F. Wang, Z. P. Li, Y. J. Mi, S. R. Yang, *Composites, Part A* **2012**, 43, 1537.
- [27] A. Georgiev, D. Dimov, E. Spasova, J. Assa, P. Dineff, G. Danev, *High Performance Polymers – Polyimides Based: From Chemistry to Applications* (Ed: M. J. M. Abadie), InTech, Sofia, Bulgaria **2012**, Chapter 4, <https://doi.org/10.5772/53918>.
- [28] R. Al-Gaashani, A. Najjar, Y. Zakaria, S. Mansour, M. A. Atieh, *Ceram. Int.* **2019**, 45, 14439.
- [29] A. Ganguly, S. Sharma, P. Papakonstantinou, J. Hamilton, *J. Phys. Chem. C* **2011**, 115, 17009.
- [30] J. F. Watts, *Surf. Interface Anal.* **1993**, 20, 267.
- [31] S. Zhao, Z. Shi, C. Wang, M. Chen, *J. Appl. Polym. Sci.* **2008**, 108, 1852.
- [32] Z. Yang, H. Peng, W. Wang, T. Liu, *J. Appl. Polym. Sci.* **2010**, 116, 2658.
- [33] W. Dai, J. Yu, Y. Wang, Y. Song, H. Bai, K. Nishimura, H. Liao, N. Jiang, *Macromol. Res.* **2014**, 22, 983.
- [34] Y. Hu, J. Jin, P. Wu, H. Zhang, C. Cai, *Electrochim. Acta* **2010**, 56, 491.
- [35] Y. Yang, T. H. Le, F. Kang, M. Inagaki, *Carbon* **2017**, 111, 546.
- [36] S. Wang, Y. Yu, R. Li, G. Feng, Z. Wu, G. Compagnini, A. Gulino, Z. Feng, A. Hu, *Electrochim. Acta* **2017**, 241, 153.
- [37] M. González-Torres, M.a. G. Olayo, G. J. Cruz, L. Ma, Gómez, V. , Sánchez-Mendieta, F. González-Salgado, *Adv. Chem.* **2014**, 2014, 965920.
- [38] O. M. Slobodian, P. M. Lytvyn, A. S. Nikolenko, V. M. Naseka, O. Y. Khyzhun, A. V. Vasin, S. V. Sevostianov, A. N. Nazarov, *Nanoscale Res. Lett.* **2018**, 13, 139.
- [39] D. David, C. Godet, *Appl. Surf. Sci.* **2016**, 387, 1125.
- [40] A. Theodosiou, B. F. Spencer, J. Counsell, A. N. Jones, *Appl. Surf. Sci.* **2020**, 508, 144764.
- [41] J. Díaz, G. Paolicelli, S. Ferrer, F. Comin, *Physical Review B – Condensed Matter and Materials Physics* **1996**, 54, 8064.
- [42] I. Kusunoki, M. Sakai, Y. Igari, S. Ishidzuka, T. Takami, T. Takaoka, M. Nishitani-Gamo, T. Ando, *Surf. Sci.* **2001**, 492, 315.
- [43] T. S. Bird, *IEEE Antennas and Propagation Magazine* **2009**, 51, 166.
- [44] A. Elrashidi, K. Elleithy, H. Bajwa, *American Journal of Polymer* **2011**.
- [45] S. Dhara, *Reviews in Plasmonic* **2015**, 2016, 275.
- [46] Y. Liu, R. Cheng, L. Liao, H. Zhou, J. Bai, G. Liu, L. Liu, Y. Huang, X. Duan, *Nat. Commun.* **2011**, 2, 577.
- [47] L. Liu, A. Das, C. M. Megaridis, *Carbon* **2014**, 69, 1.
- [48] R. Anwar, L. Mao, H. Ning, *Appl. Sci.* **2018**, 8, 1689.
- [49] R. Panwar, S. Puthucheri, D. Singh, V. Agarwala, J. R. Lee, *Adv. Compos. Mater.* **2017**, 26, 99.
- [50] B. D. Che, B. Q. Nguyen, L. T. T. Nguyen, H. T. Nguyen, V. Q. Nguyen, T. Van Le, N. H. Nguyen, *Chem. Cent. J.* **2015**, 9, 10.
- [51] L. Liang, W. Gu, Y. Wu, B. Zhang, G. Wang, Y. Yang, G. Ji, *Adv. Mater.* **2022**, 34, 2106195.
- [52] Y. Zhao, L. Hao, X. Zhang, S. Tan, H. Li, J. Zheng, G. Ji, *Small Science* **2021**, 2100077.
- [53] Z. Liao, R. Gong, Y. Nie, T. Wang, X. Wang, *Photonics Nanostruct. – Fundam. Appl.* **2011**, 9, 287.
- [54] Z. Liu, G. Bai, Y. Huang, Y. Ma, F. Du, F. Li, T. Guo, Y. Chen, *Carbon* **2007**, 45, 821.
- [55] M. H. Al-Saleh, U. Sundararaj, *J. Phys. D: Appl. Phys.* **2013**, 46, 035304.
- [56] M. K. Aswathi, A. V. Rane, A. R. Ajitha, S. Thomas, M. Jaroszewski, M. Jaroszewski, S. Thomas, A. V. Rane, *Advanced Materials for Electromagnetic Shielding*, Wiley, Hoboken, NJ, **2018**, chapter 1.
- [57] D. D. L. Chung, *Carbon* **2001**, 39, 279.

- [58] D. Chao, J. Zhang, X. Liu, X. Lu, C. Wang, W. Zhang, Y. Wei, *Polymer* **2010**, *51*, 4518.
- [59] L. Ma, G. Wang, J. Dai, *High Perform. Polym.* **2017**, *29*, 187.
- [60] A. V. Griбанov, N. A. Shirokov, Y. F. Kolpikova, G. N. Fedorova, T. I. Borisova, A. I. Koltsov, N. V. Mikhailova, L. G. Gladkova, T. Sekei, Y. N. Sazanov, *Polymer Science U.S.S.R* **1985**, *27*, 2641.
- [61] M. Inagaki, L. J. Meng, T. Ibuki, M. Sakai, Y. Hishiyama, *Carbon* **1991**, *6*, 1108.
- [62] T. Takeichi, Y. Eguchi, Y. Kaburagi, Y. Hishiyama, M. Inagaki, *Carbon* **1999**, *37*, 569.
- [63] H. Dai, M. Li, Y. Li, H. Yu, F. Bai, X. Ren, *Opt. Express* **2012**, *20*, A502.
- [64] Z. Qi, Y. Zhai, L. Wen, Q. Wang, Q. Chen, S. Iqbal, G. Chen, J. Xu, Y. Tu, *Nanotechnology* **2017**, *28*, 275202.
- [65] E. Thouti, A. K. Sharma, S. K. Sardana, V. K. Komarala, *J. Phys. D: Appl. Phys.* **2014**, *47*, 425101.